

# Innervated, Self-Sensing Liquid Crystal Elastomer Actuators with Closed Loop Control

Arda Kotikian, Javier M. Morales, Aric Lu, Jochen Mueller, Zoey S. Davidson, J. William Boley,\* and Jennifer A. Lewis\*

The programmable assembly of innervated LCE actuators (iLCEs) with prescribed contractile actuation, self-sensing, and closed loop control via core-shell 3D printing is reported. This extrusion-based direct ink writing method enables coaxial filamentary features composed of pure LM core surrounded by an LCE shell, whose director is aligned along the print path. Specifically, the thermal response of the iLCE fiber-type actuators is programmed, measured, and modeled during Joule heating, including quantifying the concomitant changes in fiber length and resistance that arise during simultaneous heating and self-sensing. Due to their reversible, high-energy actuation and their resistive feedback, it is also demonstrated that iLCEs can be regulated with closed loop control even when perturbed with large bias loads. Finally, iLCE architectures capable of programmed, self-sensing 3D shape change with closed loop control are fabricated.

to program director alignment have been limited to thin films<sup>[14,21]</sup> and 1D motifs,<sup>[13]</sup> including bulk LCEs with mechanically induced alignment.<sup>[13,22]</sup> Recently, extrusion-based 3D printing has been used to induce director alignment along the print path enabling 3D LCEs to be fabricated with programmed shape-morphing behavior, actuation response, and seamless integration with other materials.<sup>[23–26]</sup> While shape-morphing behavior has largely been achieved using light-responsive LCEs,<sup>[15,17,27]</sup> thermally responsive LCEs may be optimal actuators due to their ability to contract in response to embedded stimuli and provide sensory feedback.

## 1. Introduction

Liquid crystal elastomers (LCEs) are soft active materials that are being widely developed for soft robotics,<sup>[1–5]</sup> actuators,<sup>[6–9]</sup> and shape shifting architectures.<sup>[10–12]</sup> They are composed of a crosslinked polymer network that contains rigid mesogens, which actuate when heated above their nematic-to-isotropic transition temperature ( $T_{NI}$ ),<sup>[13,14]</sup> exposed to light,<sup>[15–17]</sup> or chemical gradients.<sup>[14,18,19]</sup> When their mesogen alignment is programmed along a specified direction, known as the director, these active materials exhibit large, reversible, and anisotropic contraction with high energy density parallel to the director.<sup>[20]</sup> Initial methods

Coupling LCEs with resistive elements that enable Joule (resistive) heating on demand has already been exploited for locomotion,<sup>[28–30]</sup> gripping,<sup>[30,31]</sup> and color change.<sup>[32,33]</sup> However, resistive heating elements are typically laminated onto unidirectionally aligned LCE films in bilayer motifs<sup>[28,29]</sup> limiting their shape, actuation mode, and function. Recently, gold serpentine-,<sup>[30,34]</sup> carbon nanoparticle-,<sup>[35]</sup> and liquid metal<sup>[33,36–38]</sup>-based heating elements have been incorporated within LCEs to induce actuation upon internally heating these composites above their  $T_{NI}$ . The intrinsically soft nature of eutectic gallium indium liquid metal (LM) elements<sup>[39–41]</sup> makes this material particularly useful for omnidirectional shape shifting, resistive self-sensing, and closed loop control strategies. Unfortunately, it is challenging to integrate LM within LCE actuators. One emerging strategy is to incorporate LM emulsions with LCEs via printing<sup>[36,38]</sup> or spray-coating.<sup>[37]</sup> However, sintered, emulsion-based LCE-LMs with complex director alignment lack the self-sensing necessary for closed loop control,<sup>[42]</sup> while spray coated LM-LCEs have only been demonstrated in the form of unidirectional actuators, whose thin LM traces are prone to electrical failure due to electromigration at the high currents required for Joule heating.<sup>[37]</sup>

Here, we report the programmable assembly of innervated LCE actuators (iLCEs) with prescribed contractile actuation, self-sensing, and closed loop control via core-shell 3D printing. This extrusion-based direct ink writing method enables coaxial filamentary features composed of pure LM core surrounded by an LCE shell, whose director is aligned along the print path (**Figure 1**). Next, we model, fabricate, and measure the thermal response of iLCE fiber-type actuators during Joule heating, including quantifying the concomitant changes in fiber length and resistance that arise during simultaneous heating and

A. Kotikian, A. Lu, Dr. J. Mueller, Dr. Z. S. Davidson, Prof. J. A. Lewis  
John A. Paulson School of Engineering and Applied Sciences  
and Wyss Institute for Biologically Inspired Engineering  
Harvard University  
Cambridge, MA 02138, USA  
E-mail: jalewis@seas.harvard.edu

J. M. Morales, Prof. J. W. Boley  
Mechanical Engineering Department  
Boston University  
Boston, MA 02215, USA  
E-mail: jwboley@bu.edu

A. Lu  
Biological Engineering Division  
Draper Laboratory  
Cambridge, MA 02139, USA

 The ORCID identification number(s) for the author(s) of this article can be found under <https://doi.org/10.1002/adma.202101814>.

DOI: 10.1002/adma.202101814

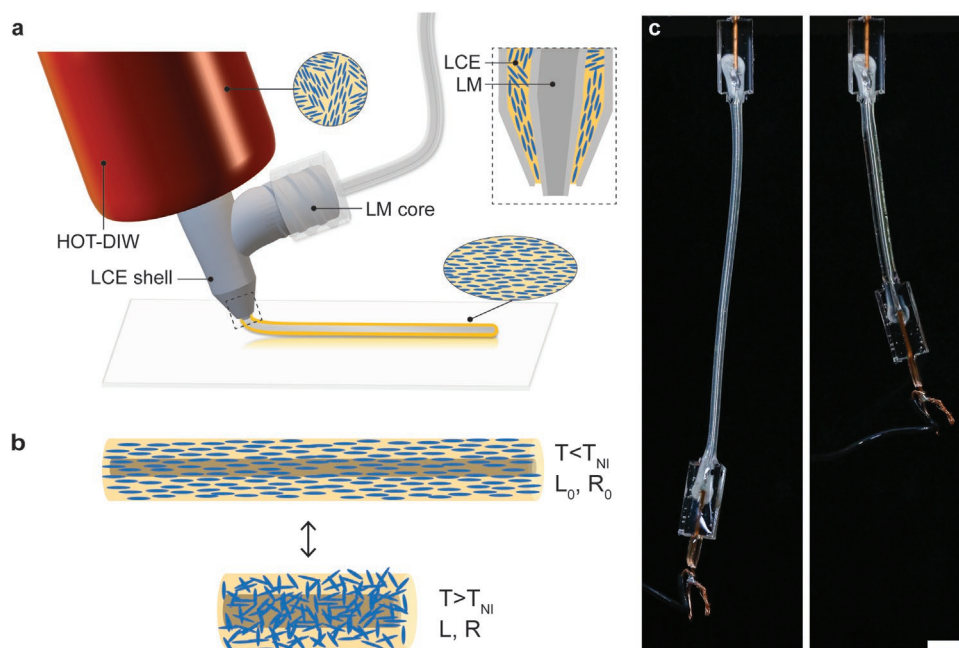


**Figure 1.** Innervated LCE fibers. a) Schematic illustration of core–shell 3D printing of iLCE fibers composed of a liquid metal (LM) core surrounded by a liquid crystal elastomer (LCE) shell, whose director is aligned along the print path. b) Schematic illustration of iLCE actuation when cycled above and below the LCE nematic-to-isotropic transition temperature,  $T_{NI}$ . c) Images of an iLCE fiber before (left) and after (right) Joule heating above  $T_{NI}$  (scale bar = 5 mm).

self-sensing. Due to their reversible, high-energy-density actuation and resistive-based sensory feedback, we then show that iLCEs can be regulated with closed loop control even when perturbed with large bias loads. Finally, we fabricate iLCE architectures capable of programmed, self-sensing 3D shape change with closed loop control.

## 2. Results and Discussion

To fabricate iLCEs, we co-extrude pure LM and a main-chain LCE ink developed previously<sup>[23–25]</sup> through a core–shell nozzle mounted on a custom-built, direct ink writing platform. Because alignment of the LCE director to a prescribed print path requires sufficient shear and extension during extrusion, the nozzle shell is retracted relative to the core<sup>[43,44]</sup> and the nozzle is tilted 20° from vertical to create a coaxial LCE (shell)–LM (core) fiber (Figure 1a and Figure S1: Supporting Information). These iLCEs are printed within the nematic phase at 25 °C and subjected to UV curing immediately upon exiting the core–shell nozzle to preserve the prescribed director alignment and the uniformity of LM deposition.<sup>[24,25,40,44]</sup> The LCE ink is over-extruded at the beginning and end of the iLCE printing process to locally disrupt director alignment in those regions thereby facilitating connection to electrical leads with minimal actuation at each end as well as sealing the LM to prevent auto-evacuation. When heated above  $T_{NI}$ , iLCEs contract in their designated print direction with correlated self-sensing (Figure 1b). Since their actuation response is gradual, we define a  $T_{NI}$  of 127 °C as the temperature at which maximum LCE actuation is first observed.<sup>[25]</sup> When iLCE fibers are heated above  $T_{NI}$  via

Joule heating, they exhibit a pronounced actuation response (Figure 1c).

We can control the actuation behavior of iLCEs by modulating the Joule heating power (Figure 2). Notably, these iLCEs exhibit uniaxial contractile strains comparable to pure 3D printed LCEs reported in our previous work<sup>[25]</sup> (Figure 2a). We normalize the power input by the initial interfacial area associated with the LM core and LCE shell regions between connection leads to enable direct comparison between printed iLCEs, where power input reflects the current input and initial resistance. We then characterized the surface temperature of the iLCE fibers at discrete power inputs (Figure 2b and Figure S2a: Supporting Information). As expected, the center of the iLCE fibers exhibits the highest temperature, which increases with power input up to a maximum value of 178.7 °C ± 4.4% at 40 mW mm<sup>-2</sup>. Importantly, core–shell printing allows iLCE fibers to be produced with relatively large LM cross-sections relative to other patterning methods, enabling high average current and low maximum voltage inputs (i.e., 9.28 A ± 5.5% at 0.5315 V ± 6.5%) and consequently elevated heat generation at attainable maximum current densities of 29.6 A mm<sup>-2</sup> ± 3.3% (40 mW mm<sup>-2</sup>) without electrical failure (Figure S2b, Supporting Information). To predict its thermal behavior, we modeled the thermal response across the cross-sectional area and length of the iLCE fibers. Given their architecture, we expected a minimal temperature gradient through the cross-section of LCE (Figure 2c) and a moderate heat gradient along the length of the fiber (Figures S3 and S4, Supporting Information). The modeled surface temperature is in good agreement to experimental maximum surface temperature (Figure 2d). Resistance decreases with heat

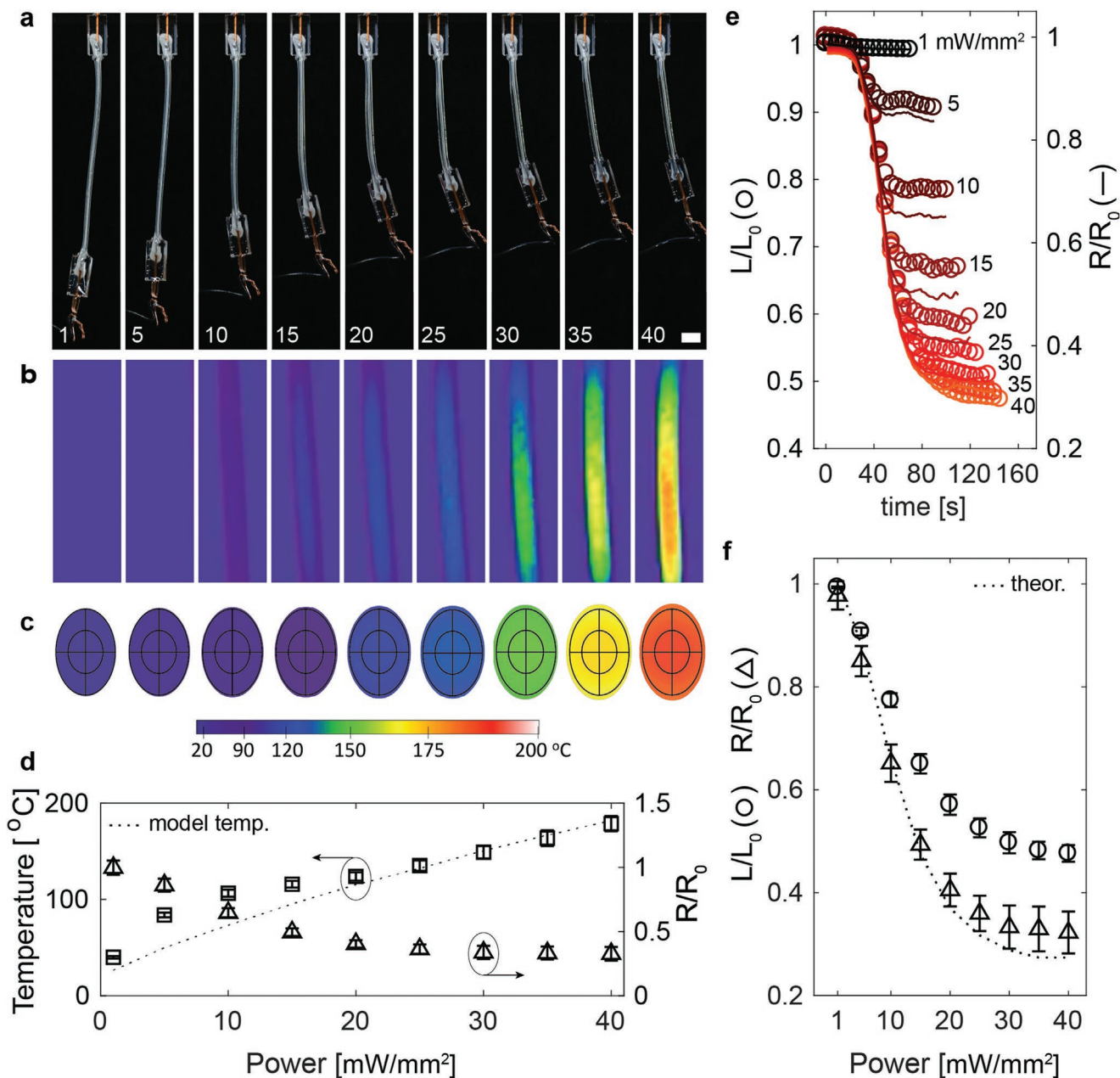


**Figure 2.** Electrothermal actuation of iLCE fibers. a,b) Optical and corresponding thermal images of representative iLCE fibers actuated with discrete power inputs ranging from 1–40 mW mm<sup>-2</sup>, which increase from left to right, as labeled (scale bar = 5 mm). c) Thermal model of the temperature across the iLCE fiber (cross-section) at these discrete power inputs, where inner and outer black outlines indicate initial dimensions of LM and LCE, respectively. d) Measured surface temperature, surface temperature extracted from thermal model, and average  $R/R_0$  of iLCEs at these discrete power inputs. e)  $L/L_0$  and  $R/R_0$  with respect to time of a representative iLCE at these discrete power inputs. f) Average  $L/L_0$ , average  $R/R_0$ , and theoretical  $R/R_0$  modeled with Ohm's law with resistivity temperature correction for discrete power inputs. [Note: Error bars indicate standard deviations.]

due to the change in geometry of the actuator, with a plateau in normalized resistance ( $R/R_0$ ) above 25 mW mm<sup>-2</sup>, also corresponding to the power at which entire iLCE fiber is expected to be above its  $T_{NI}$  (127 °C) (Figure 2d and Figure S4, Supporting Information).

Next, we investigated the programmable shape change and predictable self-sensing performance of these iLCE fibers. As

expected, their actuation at different power inputs shows that  $R/R_0$  is closely correlated with normalized length ( $L/L_0$ ) during Joule heating (Figure 2e and Movie S1: Supporting Information) and also with cooling (Figure S2c, Supporting Information). Hence, changes in  $L/L_0$  and  $R/R_0$  are dependently programmable with power input (Figure 2f), i.e., greater contractile strain results in greater decrease in resistance. Since

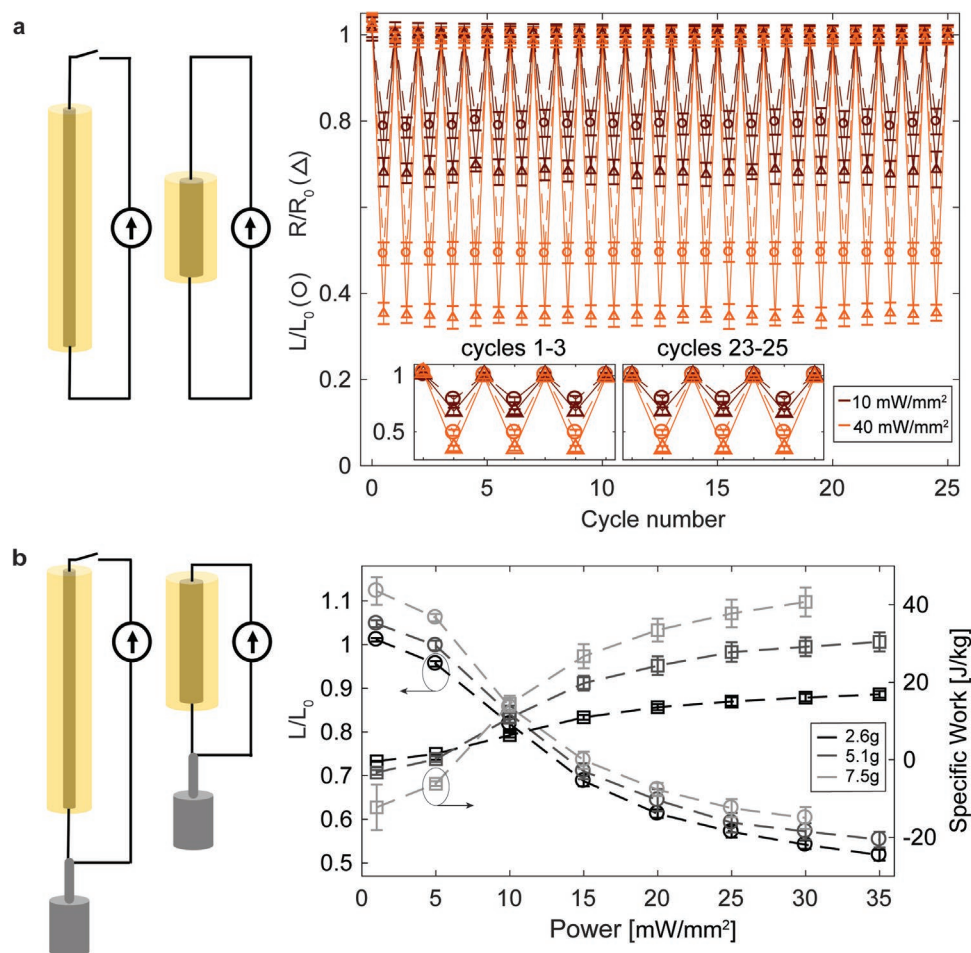


**Figure 3.** Performance of iLCE fiber actuators. a) Scheme of reversible iLCE actuation (left) and plot of measured  $L/L_0$  and  $R/R_0$  when cycled at low ( $10 \text{ mW mm}^{-2}$ ) and high ( $40 \text{ mW mm}^{-2}$ ) power inputs (right). b) Scheme of iLCEs lifting weight (left) and plot of measured  $L/L_0$  and specific work (work by LCE mass) when lifting different weights at discrete power inputs (right). [Note: Error bars indicate standard deviations.]

resistance depends on both geometry and temperature, it can be predicted taking the temperature generated and strain of iLCEs at discrete power inputs (Equation (1)), accounting for both the change in geometry and temperature, where  $\alpha$  is the temperature coefficient of resistivity.

$$\frac{R}{R_0} = [1 + \alpha(T - T_0)] \left( \frac{L}{L_0} \right)^2 \quad (1)$$

To achieve more reliable changes in  $L/L_0$  and  $R/R_0$ , the current is ramped up and down. However, iLCEs can be rapidly actuated by applying a step input power of  $40 \text{ mW mm}^{-2}$ , in which over 90% of their maximum contractile strain is attained within 10 s (Figure S2d, Supporting Information).

To characterize actuator performance, we explored iLCE actuation strain repeatability and work output (Figure 3). When cycled between on and off states 25 times, iLCEs exhibit average  $L/L_0 = 0.79 \pm 0.5\%$  and  $R/R_0 = 0.68 \pm 0.7\%$  or  $L/L_0 = 0.49 \pm 0.1\%$  and  $R/R_0 = 0.35 \pm 0.9\%$  for low (i.e.,  $10 \text{ mW mm}^{-2}$ ) and high power (i.e.,  $40 \text{ mW mm}^{-2}$ ) on states, respectively (Figure 3a and Figure S5, Movie S2: Supporting

Information). Notably, iLCEs demonstrate repeatable programming of  $L/L_0$  and resulting  $R/R_0$  at both partial and full actuation, which are closely correlated throughout the duration of the power profile used (Figure S5, Supporting Information). Next, we Joule heated iLCEs at several power inputs and bias loads in weight-lifting experiments. Akin to unstressed iLCE experiments, increasing power input results in larger strains, but decreases with larger bias loads (Figure 3d). Work exertion increases with both power input and bias load (Figure 3d). We find that  $30 \text{ mW mm}^{-2}$  power and  $7.5 \text{ g}$  bias load are the maximum power and loading conditions that these iLCEs can reliably lift. Upon heating, LCE actuators increase in length prior to contracting with sufficient bias loads, as observed for other LCEs that are not monodomain (Figure S6, Supporting Information).<sup>[24,45]</sup> If total contraction results in length greater than the initial unbiased length ( $L_0$ ), it is defined as an extension (i.e.,  $L/L_0 > 1$ ) and negative work output. Overall, iLCEs lift bias loads over 200x their own LCE weight, with maximum specific work ( $40.7 \text{ J kg}^{-1} \pm 9.1\%$ ) comparable to our prior observations for pure LCEs.<sup>[25]</sup> To further increase their work output, cross-sectional area of the active material can be increased either by

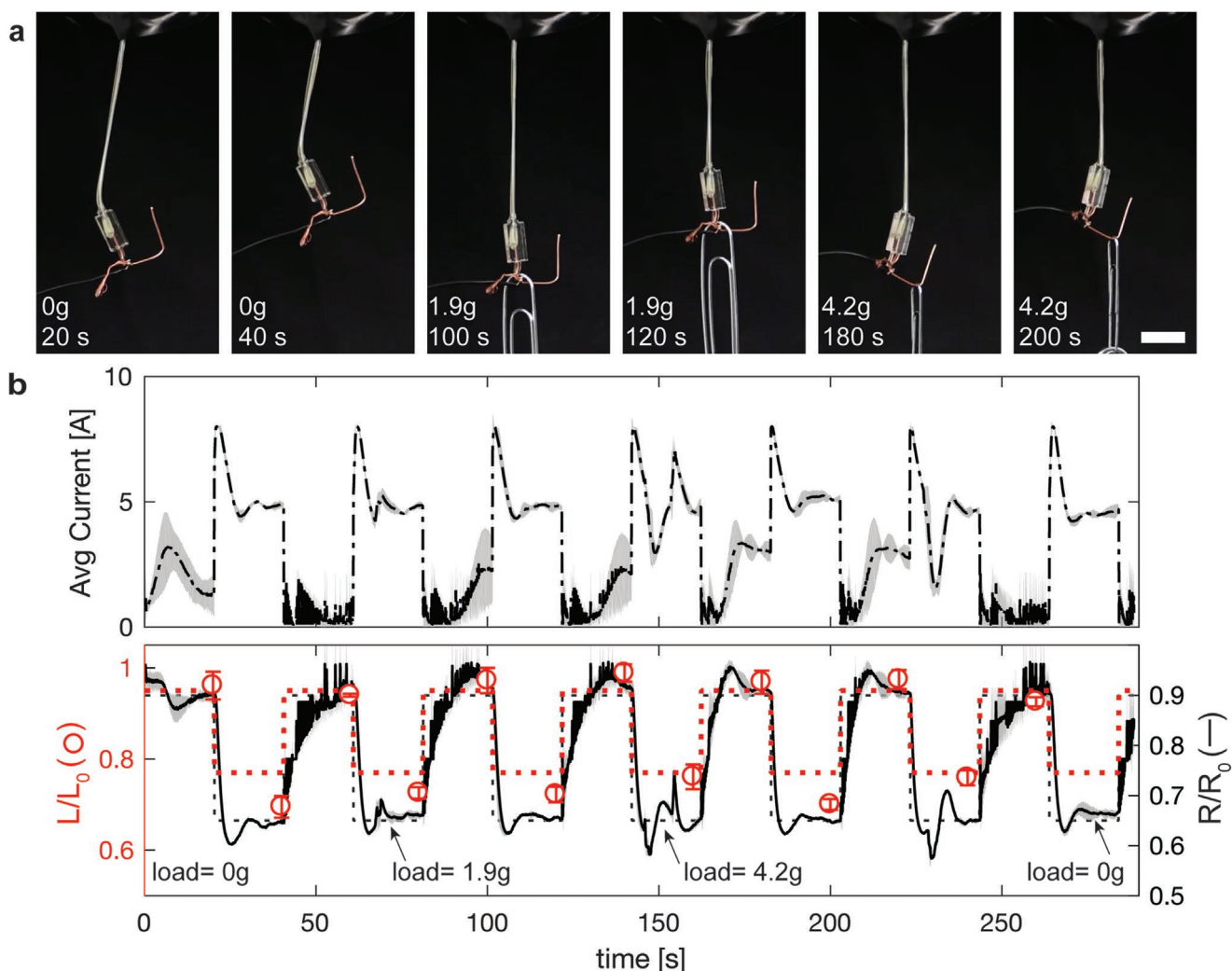


**Figure 4.** Closed loop control of iLCE fiber actuation. a) Optical images of a representative iLCE fiber with self-adjusting actuation under several loading conditions (scale bar = 10 mm). b) Self-adjusting current profile (top) and change in resistance and length (bottom) as a function of time for iLCE fibers that are perturbed with bias loads, while reaching target values of resistance (black, dashed) and corresponding length (red, dashed). [Note: Lines denote average values, while shaded regions or error bars indicate standard deviations.]

printing bundled iLCE fibers or patterning pure LCEs alongside these fiber(s) via multimaterial 3D printing.

Given that iLCEs are able to reversibly actuate with self-sensing capabilities and exert substantial work, we explored regulating their actuation response via closed loop control (Figure 4). Specifically, a control system is programmed with a target  $R/R_0$  that autoregulates iLCE resistance feedback to reach the target over time, even with bias stress perturbations (Figure 4a and Figure S7: Supporting Information). We designate a target resistance square wave with two targets  $R/R_0 = 0.90$  and  $R/R_0 = 0.65$  for 20 s each, corresponding to target contractile strains of  $\approx 5\%$  and 23%, respectively. The current rapidly self-adjusts without manual intervention, such that the  $R/R_0$  values of the iLCEs lie within the target resistance curve with 3.1% and 4.5% overshoot and undershoot, respectively. Importantly, our iLCE actuators are capable of tracking self-sensing actuation while rejecting disturbances up to 4.2 grams ( $>115\times$  the LCE weight) within 20 s (Figure 4b and Figure S7: Supporting Information).

As a final demonstration, we fabricated iLCE spirals with 2D director patterning via 3D printing to achieve a programmable out-of-plane shape change (Figure 5). Specifically, we patterned the iLCE with a square spiral print path, which is expected to actuate into a cone when heated above  $T_{NI}$ .<sup>[14,24]</sup> Like its fiber actuator counterparts, spiral iLCEs are repeatedly actuated via Joule heating and output a corresponding change in resistance. At low power input ( $5\text{ mW mm}^{-2}$ ), a fraction of the iLCE actuates and forms a partial cone, corresponding to a maximum height of  $8.77\text{ mm} \pm 1.9\%$  with corresponding  $R/R_0$  of  $0.63 \pm 2.0\%$  (Figure 5a,b and Movie S4: Supporting Information). At higher power input ( $15\text{ mW mm}^{-2}$ ) almost the entire structure is above  $T_{NI}$  and actuates into a full cone with a maximum height of  $12.29\text{ mm} \pm 1.6\%$  and corresponding  $R/R_0$  of  $0.35 \pm 1.5\%$  (Figure 5c,d and Movie S4: Supporting Information). We note that the frequency of cycling current is slow to allow cooling of the large structure, with cycles 2–4 shown in Figure 5 (Figure S8, Supporting Information). With sufficient

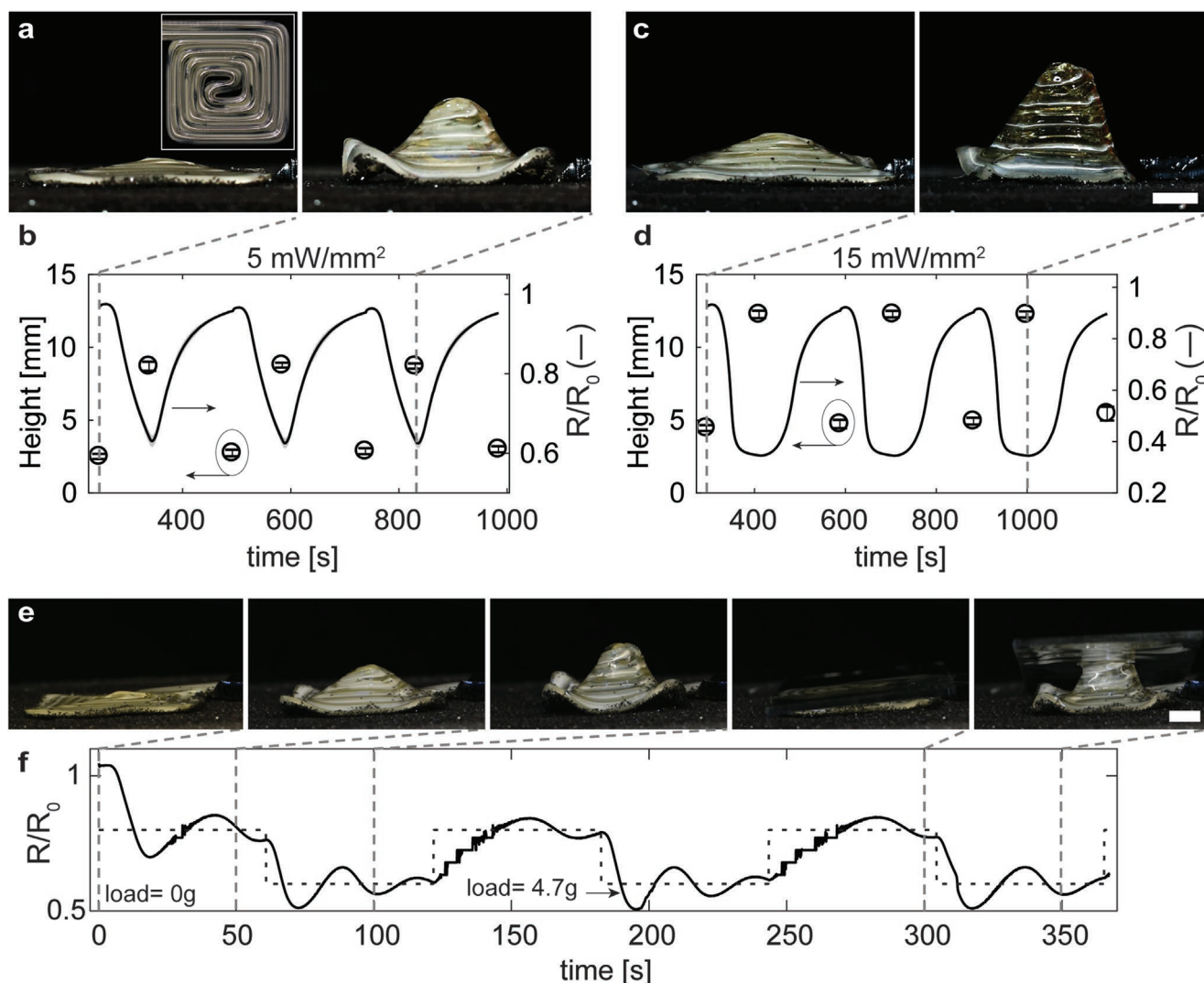


**Figure 5.** 3D actuation of iLCE spiral architectures with closed loop control. a) Side-view images of a printed iLCE when cycled between off ( $0 \text{ mW mm}^{-2}$ , left) and on ( $5 \text{ mW mm}^{-2}$ , right) power input. [A top-view image of the printed iLCE spiral architecture (off state) is shown in the inset.] b) Average height and resistance profile of printed iLCE spiral architectures cycled at a power input of  $5 \text{ mW mm}^{-2}$ . c) Side-view images of a printed iLCE when cycled between off ( $0 \text{ mW mm}^{-2}$ , left) and on ( $15 \text{ mW mm}^{-2}$ , right) power input. d) Average height and resistance profile as a function of time for printed iLCE spiral architectures cycled at  $15 \text{ mW mm}^{-2}$  power. [Note: The plots do not include the first cycle.] e) Image sequence of a printed iLCE spiral architecture and f) resistance profile of actuation as a function of time with closed loop control (bottom), where the target resistance is shown as a dashed line (scale bars = 5 mm). [Note: Lines denote average values, while shaded regions or error bars indicate standard deviations.]

time to cool, the spiral iLCEs return to a flat shape and within 5% of the initial  $R/R_0$ . The reversible and large change in resistance corresponding to the change in height enables closed loop control of 3D shape change (Figure 5e,f and Movie S5: Supporting Information). Here, we program a target resistance curve with 60 s intervals at  $R/R_0 = 0.8$  and  $R/R_0 = 0.6$  and the iLCE spiral actuates to these targets both with and without a bias load (4.7 g). Longer time intervals relative to those of iLCE fibers are necessary due to the scale of the iLCE spiral and ensuing timescale of heat dissipation. This capability could be deployed in the future to create reconfigurable iLCE-based antennae with closed loop control, and, hence, tunable RF properties.<sup>[11]</sup>

### 3. Conclusion

We have fabricated innervated LCEs with programmable actuation, self-sensing, and closed loop control via core-shell 3D printing. Importantly, our approach enables pure liquid metal cores to be directly embedded within LCE-based coaxial fibers. We demonstrated that these iLCE fibers exhibit prescribed and predictable thermal responses, strain, and self-sensing upon Joule heating, with strains of nearly 50% when heated above their nematic-to-isotropic transition temperature. Programmability, repeatability, magnitude of sensing signal, and large work output enabled closed loop control of printed 1D iLCE fibers and 2D-to-3D shape-morphing architectures. With further

development, iLCE architectures in arbitrary designs could be printed and controlled in a closed loop system for use in intelligent soft robotics, reconfigurable soft electronics, and RF devices.

## 4. Experimental Section

**Materials:** The LCE ink is prepared using an aza-Michael addition method, which was reported previously.<sup>[25]</sup> A 1.1:1 molar ratio of 1,4-bis-[4-(6-acryloyloxy-hexyloxy)benzoyloxy]-2-methylbenzene (Wilshire Technologies Inc.) and n-butylamine (Sigma-Aldrich), 0.2 wt% butylated hydroxy toluene (Fisher Scientific), and 2 wt% Irgacure 651 (BASF) was combined, stirred, and heated at 105 °C for 18 h in the absence of light. The ink was transferred to a custom stainless-steel barrel and degassed in a vacuum oven (VWR) overnight prior to printing. A liquid metal (LM) ink composed of eutectic gallium indium (5N Plus) was used as-received.

**Core-Shell 3D Printing:** Core-shell nozzles were first produced using stereolithography (Perfactory Aureus, Envisiontec) and subsequently coated with 1H,1H,2H,2H-perfluorooctyltriethoxysilane (FOTS, Oakwood Chemical) to minimize crosslinking with the LCE ink. The nozzle dimensions are provided in Figure S9 (Supporting Information). The LCE ink was extruded through the outer shell of the coaxial nozzle by applying pressure (Ultimus V, Nordson EFD). A polyimide flexible heater (McMaster-Carr) was wrapped around the nozzle to maintain a constant temperature of 25 °C. The LM ink was extruded through the inner core of the nozzle using a syringe pump (PHD Ultra, Harvard Apparatus). During printing, the core-shell printhead was tilted 20° from the vertical axis to improve printability of innervated LM (core)-LCE (shell) architectures, referred to as iLCEs. These iLCE have ellipsoidal cross-sections, with initial major and minor diameters of  $1.34 \pm 0.12$  mm  $\times$   $0.93 \pm 0.08$  mm and  $0.702 \pm 0.04$  mm  $\times$   $0.571 \pm 0.05$  mm for the LCE shell and LM core, respectively.

iLCEs were printed in the form of 1D coaxial fibers and 2D-to-3D shape morphing structures using a custom-built, three-axis motion controlled stage (Aerotech Inc.) equipped with on-the-fly UV crosslinking at  $\approx 8$  mW cm<sup>-2</sup> intensity (Omnicure, S2000). iLCEs fibers and spiral-based planar structures were printed on poly(vinyl alcohol) (80% hydrolyzed, Aldrich)-coated glass substrates or pre-cleaned glass substrates (VWR), respectively, to allow release from the substrate without deformation. Spiral iLCEs were printed on a rotary stage (Aerotech Inc.), since the tilted nozzle prevents extrusion in both positive and negative x-directions. iLCE fibers were typically printed by extruding the LCE ink at an applied pressure of 3.6 MPa and the LM ink at a flow rate of 0.0197 mL min<sup>-1</sup> with a print speed of 2 mm s<sup>-1</sup> and a print height of 0.25 mm. Spiral iLCEs were printed with a 1.7 mm center-to-center spacing between filaments under the same conditions, except at a reduced print speed of 0.85 mm s<sup>-1</sup>. At the start and end of each printed iLCE, the LCE ink was over-extruded by reducing the print speed by a factor of 2 as the nozzle was translated for 5 mm in the desired direction. After printing, the iLCEs were fully crosslinked by an additional UV exposure step of  $\geq 30$  min in duration on each side (S2000, Omnicure;  $\approx 5$  mW cm<sup>-2</sup>).

As a final step, a 23 AWG copper wire (Diji-Key Corp.) was mechanically filed, inserted in the iLCEs, connected to their LM core, and sealed with an adhesive (NOA 68, Norland Inc.) that promotes bonding upon crosslinking with UV light (S2000, Omnicure; minimum 300 s). A 28 AWG compliant lead wire (Diji-Key Corp.) of roughly 10 cm length was then soldered onto one end of iLCE fibers as to not affect LCE  $L/L_0$  and  $R/R_0$  (Figure S10, Supporting Information). Spiral iLCEs did not require a lead wire. During their 2D-to-3D shape morphing, these architectures were imaged on a layer of black craft sand (Just Artifacts) on super-cushioning polyurethane foam (McMaster-Carr) to minimize friction, adhesion, and thermal diffusion with the substrate upon cooling.

**Electrothermal Testing:** To electrothermally (Joule) heat and measure the resistance of iLCE actuators, programmed current was provided via a power supply (2230G-30-6, Keithley) and voltage was measured at 1 s intervals using a multimeter (34405A, Agilent) (Figure S10, Supporting Information). The power source and multimeter were controlled in parallel by a custom MATLAB script. The resistance  $R$  was normalized by the initial resistance  $R_0$  of the iLCE (RM3544-01, HIOKI) to determine the normalized resistance,  $R/R_0$ . The length  $L$  was normalized to the initial length  $L_0$  (in pixels) to determine the normalized length,  $L/L_0$ . The power input, which was normalized by the total interfacial area between the LM (core) and LCE (shell), was calculated from the initial resistance, the LM length between leads, and the elliptical cross-sectional area, where the major and minor diameters were estimated from imaging the top and side of the printed core-shell filament (SteREO Discovery V20 Microscope, Zeiss). The power input of spiral iLCEs was normalized by the total interfacial area estimated from the initial resistance (RM3544-01, HIOKI) and assuming a circular LM cross-section to account for disparities in cross-sectional area of LM along the edges and corners of the spiral.

All the electrothermal tests on the iLCE fibers were repeated with identical current profiles on the leads replicated without the fiber, which included the compliant lead wire and copper connection lead of the same lengths. The measured resistance of the leads was subtracted from the total resistance to obtain the resistance of neat iLCE. All the iLCE fibers were subjected to a current profile that consisted of ramping up the current in 0.5 A increments (with 5 s hold at each step) to the peak value required for a given power input (on state), holding in this state for 60 s, then ramping down the current in 0.5 A increments (with 5 s hold at each step), and, finally, holding the current at 0.5 A for 60 s (off state), unless otherwise noted. Cycling experiments were conducted using the same current profiles, in which the peak current values were held for 30 s. Note, the off resistance of these iLCE fibers was measured at a current of 0.5 A, i.e., under conditions without significant heat input. Similarly, for spiral iLCEs, an off state was at 0.1 A. Spiral iLCEs were tested with 0.1 A per 1 s ramps, and cycled 4 $\times$  with current holds of 60 and 120 s at the on and off states, respectively. Peak on currents of 2.813 and 4.873 A were applied for 5 and 15 mW mm<sup>-2</sup> power inputs, respectively.

**Finite Element Modeling:** The 3D thermal-mechanical model consisted of a transient study with solid mechanics and heat transfer modules (Comsol Multiphysics), where the geometry of the device was based on the average dimensions of the iLCE fiber. The heat source for the model was set as joule heating through the core of the iLCEs. Heat losses were assumed to occur by natural convection and a correlation for thin vertical cylinders was implemented to determinate the Nusselt number of the heated surface across space and time.<sup>[46]</sup> Values for LM thermal conductivity ( $k = 26.4$  W m<sup>-1</sup> K<sup>-1</sup>), specific heat ( $c_p = 333.75$  J kg<sup>-1</sup> K<sup>-1</sup>), density ( $d = 6250$  kg m<sup>-3</sup>), resistivity ( $\rho = 2.79 \times 10^{-7}$   $\Omega$  m), and coefficient of thermal expansion (CTE =  $32.97 \times 10^{-6}$  K<sup>-1</sup>) and LCE specific heat ( $c_p = 1000$  J kg<sup>-1</sup> K<sup>-1</sup>) and density ( $d = 1200$  kg m<sup>-3</sup>) were estimated from the literature.<sup>[36,47,48]</sup> The LCE thermal conductivity ( $k$ ), coefficient of thermal expansion (CTE), and mechanical properties (Figure S3, Supporting Information) were experimentally measured on printed LCE samples, as described below.

**LCE Characterization:** Thermal conductivity ( $k$ ) was measured with a thermal conductivity analyzer (CTi, C-Therm) on a printed LCE in a temperature test chamber (TJR-A-F4T, Tenney). To reach thermal equilibrium between measurements, the test chamber was held at target temperatures for 10 min, with measurements taken every 60 s. The coefficient of thermal expansion (CTE) was measured via a dilatometer (DiL, C-Therm) both parallel and perpendicular to the director of printed LCEs with approximate dimensions of  $5 \times 5 \times 2$  mm<sup>3</sup> with a heating rate of 2 °C min<sup>-1</sup>. The data were processed using the ASTM E0229-17 standard. Mechanical testing was conducted on printed LCE perpendicular bilayers with approximate dimension of  $30 \times 5 \times 0.4$  mm<sup>3</sup> (Instron 5566, 100 N load cell). The mechanical deformation was modeled by the 5-parameters hyperelastic Mooney-Rivlin Model,<sup>[49]</sup> where appropriate parameters for the mechanical model

were determined by optimization via the Levenberg–Marquardt method (Figure S3, Supporting Information).

**Actuation Characterization:** Images used to measure length were captured (EOS Rebel T2i, Canon) every 5 s for iLCE fibers and every 1 s for spiral iLCEs and analyzed using image analysis software (Fiji) and a custom Python script. The iLCE actuators used for thermal imaging were first spray painted with a thin coat of graphite paint (Bonderite L-GP G Acheson) to prevent errors in surface temperature measurement arising from the nematic to isotropic phase transition. Thermal imaging was carried out using an IR camera (SC5000, FLIR) and their temperature was calculated (Altair) using an emissivity of 0.95. The thermal images, provided in Figure 2b, correspond to the end of the peak current time for the on state of each condition.

Average values of normalized resistance, normalized length, and work for each printed iLCE fiber tested were averaged over the second half of peak current input (e.g., for a peak hold of 60 s, the measured values at 30–60 s would be averaged). Bias load was applied to the actuators by adding paperclips to the bottom of the actuator. Weight-lifting experiments were conducted starting at low power then increasing to high power for each load and actuating at 35 mW mm<sup>-2</sup> without weight between loads to erase the thermal history. Specific work was calculated with respect to the average mass of LCE (35 mg ± 2 mg), estimated from the cross-sectional dimensions across 50 mm of fiber and taking the density of LCE as 1.08 g mL<sup>-1</sup>. The average height of spiral iLCEs was acquired at the end of the peak current time for on and off states.

**Closed Loop Control:** The PID closed loop control was implemented using a custom script (Python 2.7) to program electrical current and measure the voltage drop across the iLCEs (E36233a, Keysight). The target  $R/R_0$  was inputted in the control script and the target  $L/L_0$  estimated given the target  $R/R_0$  and the electrothermal actuation characterization (Figure 2f). The sampling rate of the loop was set to be 1000 Hz, which is 4 orders of magnitude faster than the thermal response of the iLCE. PID gains were estimated using the system identification toolbox (MATLAB). For iLCE fibers, the PID gains ( $K_p$ ,  $K_d$ , and  $K_i$ ) were found to be 22, 21, and 0.9 respectively. For the spiral iLCEs, the PID gains ( $K_p$ ,  $K_d$ , and  $K_i$ ) were found to be 2.5, 2, and 0.001 respectively. The target step lengths of iLCE fibers and spiral architecture were 20 and 60 s, respectively. Images used to measure length of the control response were captured (Nikon D850) every 2 s for iLCE fibers and every 1 s for spiral iLCEs and analyzed for length using image analysis software (After Effects, Adobe) and a custom Python script.

## Supporting Information

Supporting Information is available from the Wiley Online Library or from the author.

## Acknowledgements

The authors gratefully acknowledge support from the National Science Foundation through the Harvard MRSEC (DMR-2011754; A.K., J.L.), the ARO MURI (W911NF-17-1-03; Z.D., J.L.), NSF DMRREF (DMR-1922321; J.M., J.L.), and the AFOSR Young Investigator Award (FA9550-20-1-0365; J.W.B., J.M.M.). A.L. gratefully acknowledges support provided by a Draper Lab fellowship. This work made use of the Shared Experimental Facilities supported in part by the Harvard MRSEC. The authors thank E. Guzman, S.C. Slimmer, N. Larson, J. P. S. Aquino, S. F. Zopf, and M. Horenstein for helpful discussions, J. Alvarenga for technical assistance, and L.K. Sanders for assistance with videography.

## Conflict of Interest

The authors declare no conflict of interest.

## Data Availability Statement

The data that support the findings of this study are available from the corresponding author upon reasonable request.

## Keywords

3D printing, liquid crystal elastomers, actuators, shape morphing

Received: March 7, 2021

Revised: April 1, 2021

Published online:

- [1] D. Rus, M. T. Tolley, *Nature* **2015**, 521, 467.
- [2] T. J. Wallin, J. Pikul, R. F. Shepherd, *Nat. Rev. Mater.* **2018**, 3, 84.
- [3] S. W. Ula, N. A. Traugott, R. H. Volpe, R. R. Patel, K. Yu, C. M. Yakacki, *Liq. Cryst. Rev.* **2018**, 6, 78.
- [4] M. Wehner, R. L. Truby, D. J. Fitzgerald, B. Mosadegh, G. M. Whitesides, J. A. Lewis, R. J. Wood, *Nature* **2016**, 536, 451.
- [5] Y. Y. Xiao, Z. C. Jiang, X. Tong, Y. Zhao, *Adv. Mater.* **2019**, 31, 1903452.
- [6] J. M. McCracken, B. R. Donovan, T. J. White, *Adv. Mater.* **2020**, 32, 1906564.
- [7] L. Hines, K. Petersen, G. Z. Lum, M. Sitti, *Adv. Mater.* **2017**, 29, 1603483.
- [8] C. Ohm, M. Brehmer, R. Zentel, *Adv. Mater.* **2010**, 22, 3366.
- [9] J. Liu, Y. Gao, H. Wang, R. Poling-Skutvik, C. O. Osuji, S. Yang, *Adv. Intell. Syst.* **2020**, 2, 1900163.
- [10] X. Kuang, D. J. Roach, J. Wu, C. M. Hamel, Z. Ding, T. Wang, M. L. Dunn, H. J. Qi, *Adv. Funct. Mater.* **2018**, 29, 1805290.
- [11] J. W. Boley, W. M. Van Rees, C. Lissandrello, M. N. Horenstein, R. L. Truby, A. Kotikian, J. A. Lewis, L. Mahadevan, *Proc. Natl. Acad. Sci. USA* **2019**, 116, 20856.
- [12] K. Bertoldi, V. Vitelli, J. Christensen, M. Van Hecke, *Nat. Rev. Mater.* **2017**, 2, 17066.
- [13] J. Kupfer, H. Finkelmann, *Makromol. Chem., Rapid Commun.* **1991**, 12, 717.
- [14] T. H. Ware, M. E. McConney, J. J. Wie, V. P. Tondiglia, T. J. White, *Science (80-)* **2015**, 347, 982.
- [15] A. W. Hauser, D. Liu, K. C. Bryson, R. C. Hayward, D. J. Broer, *Macromolecules* **2016**, 49, 1575.
- [16] Y. Yu, M. Nakano, T. Ikeda, *Nature* **2003**, 425, 145.
- [17] S. Palagi, A. G. Mark, S. Y. Reigh, K. Melde, T. Qiu, H. Zeng, C. Parmeggiani, D. Martella, A. Sanchez-Castillo, N. Kapernaum, F. Giesselmann, D. S. Wiersma, E. Lauga, P. Fischer, *Nat. Mater.* **2016**, 15, 647.
- [18] K. D. Harris, C. W. M. Bastiaansen, D. J. Broer, *J. Microelectromech. Syst.* **2007**, 16, 480.
- [19] J. M. Boothby, H. Kim, T. H. Ware, *Sens. Actuators, B* **2017**, 240, 511.
- [20] T. J. White, D. J. Broer, *Nat. Mater.* **2015**, 14, 1087.
- [21] H. Aharoni, Y. Xia, X. Zhang, R. D. Kamien, S. Yang, *Proc. Natl. Acad. Sci. USA* **2018**, 115, 7206.
- [22] C. M. Yakacki, M. Saed, D. P. Nair, T. Gong, S. M. Reed, C. N. Bowman, *RSC Adv.* **2015**, 5, 18997.
- [23] C. Ambulo, J. J. Burroughs, J. M. Boothby, H. Kim, M. R. Shankar, T. H. Ware, *ACS Appl. Mater. Interfaces* **2017**, 9, 37332.
- [24] A. Kotikian, R. L. Truby, J. W. Boley, T. J. White, J. A. Lewis, *Adv. Mater.* **2018**, 30, 1706164.
- [25] A. Kotikian, C. McMahan, E. C. Davidson, J. M. Muhammad, R. D. Weeks, C. Daraio, J. A. Lewis, *Sci. Robot.* **2019**, 4, eaax7044.

- [26] M. O. Saed, C. P. Ambulo, H. Kim, R. De, V. Raval, K. Searles, D. A. Siddiqui, J. M. Cue, D. C. Rodrigues, M. C. Stefan, R. Shankar, T. H. Ware, *Adv. Funct. Mater.* **2019**, *29*, 1806412.
- [27] A. H. Gelebart, D. Jan Mulder, M. Varga, A. Konya, G. Vantomme, E. W. Meijer, R. L. B. Selinger, D. J. Broer, *Nature* **2017**, *546*, 632.
- [28] C. Yuan, D. J. Roach, C. K. Dunn, Q. Mu, X. Kuang, C. M. Yakacki, T. J. Wang, K. Yu, H. J. Qi, *Soft Matter* **2017**, *13*, 5558.
- [29] C. Wang, K. Sim, J. Chen, H. Kim, Z. Rao, Y. Li, W. Chen, J. Song, R. Verduzco, C. Yu, *Adv. Mater.* **2018**, *30*, 1706695.
- [30] Q. He, Z. Wang, Y. Wang, A. Minori, M. T. Tolley, S. Cai, *Sci. Adv.* **2019**, *5*, eaax5746.
- [31] D. J. Roach, X. Kuang, C. Yuan, K. Chen, H. J. Qi, *Smart Mater. Struct.* **2018**, *27*, 125011.
- [32] Y. Jiang, D. Xu, X. Li, C. Lin, W. Li, Q. An, C. Tao, H. Tang, G. Li, *J. Mater. Chem.* **2012**, *22*, 11943.
- [33] B. Ma, C. Xu, L. Cui, C. Zhao, H. Liu, *ACS Appl. Mater. Interfaces* **2021**, *13*, 5574.
- [34] J. M. Boothby, J. C. Gagnon, E. Mcdowell, T. Van Volkenburg, L. Currano, Z. Xia, *Soft Rob.* **2021**, <https://doi.org/10.1089/soro.2020.0135>.
- [35] M. Chambers, H. Finkelmann, M. Remškar, A. Sánchez-Ferrer, B. Zalar, S. Žumer, *J. Mater. Chem.* **2009**, *19*, 1524.
- [36] M. J. Ford, C. P. Ambulo, T. A. Kent, E. J. Markvicka, C. Pan, J. Malen, T. H. Ware, C. Majidi, *Proc. Natl. Acad. Sci. USA* **2019**, *116*, 21438.
- [37] T. A. Kent, M. J. Ford, E. J. Markvicka, C. Majidi, *Multifunct. Mater.* **2020**, *3*, 025003.
- [38] C. P. Ambulo, M. J. Ford, K. Searles, C. Majidi, T. H. Ware, *ACS Appl. Mater. Interfaces* **2020**, *13*, 12805.
- [39] M. D. Dickey, R. C. Chiechi, R. J. Larsen, E. A. Weiss, D. A. Weitz, G. M. Whitesides, *Adv. Funct. Mater.* **2008**, *18*, 1097.
- [40] T. V. Neumann, M. D. Dickey, *Adv. Mater. Technol.* **2020**, *5*, 2000070.
- [41] L. Yu, J. C. Yeo, R. H. Soon, T. Yeo, H. H. Lee, C. T. Lim, *ACS Appl. Mater. Interfaces* **2018**, *10*, 12773.
- [42] E. J. Markvicka, M. D. Bartlett, X. Huang, C. Majidi, *Nat. Mater.* **2018**, *17*, 618.
- [43] M. A. H. Khondoker, A. Ostashek, D. Sameoto, *Adv. Eng. Mater.* **2019**, *21*, 1900060.
- [44] K. Wu, P. Zhang, F. Li, C. Guo, Z. Wu, *Polymers (Basel)* **2018**, *10*, 330.
- [45] M. O. Saed, A. H. Torbati, C. A. Starr, R. Visvanathan, N. A. Clark, C. M. Yakacki, *J. Polym. Sci., Part B: Polym. Phys.* **2017**, *55*, 157.
- [46] A. Bejan, *Convection Heat Transfer*, John Wiley & Sons, Hoboken, NJ, USA **2013**.
- [47] M. D. Bartlett, N. Kazem, M. J. Powell-palm, X. Huang, W. Sun, *Proc. Natl. Acad. Sci. USA* **2017**, *114*, 2143.
- [48] S. Liu, M. C. Yuen, E. L. White, J. W. Boley, B. Deng, G. J. Cheng, R. Kramer-Bottiglio, *ACS Appl. Mater. Interfaces* **2018**, *10*, 28232.
- [49] N. Kumar, V. V. Rao, *MIT Int. J. Mech. Eng.* **2016**, *6*, 43.